Available online at www.sciencedirect.com
ScienceDirect
Trans. Nonferrous Met. Soc. China 31(2021) 2307−2322
Transactions of Nonferrous Metals Society of China
www.tnmsc.cn

Effect of initial deposition behavior on properties of electroless Ni−P coating on ZK60 and ME20 magnesium alloys

Li FENG, You-wei ZHANG, Chen WEN, Si-zhen LI, Jia-feng LI, De CHENG, Jing-ying BAI, Qing-xin CUI, Li-gong ZHANG

Beijing Spacecraft, China Academy of Space Technology, Beijing 100194, China

Received 4 August 2020; accepted 21 May 2021

Abstract: The composition of magnesium alloys is greatly associated with initial deposition behavior of electroless Ni−P coatings. Thus, the initial deposition behavior of electroless Ni–P coatings on ZK60 and ME20 alloys was investigated. The results indicated that differences in the alloy compositions significantly influenced the initial deposition process and the adhesive strength, corrosion resistance, and crystal structure. The initial deposition of coatings on ZK60 and ME20 alloys preferentially occurred on the precipitates. The precipitates in ZK60 alloy had higher chemical activity after HF activation and controlled the initial deposition rate of the coating. The initial deposition rate of the coating on ME20 alloy mainly depended on the density of the MgF_2 film formed by HF activation rather than on the precipitates. Owing to differences in the initial deposition process, the coating on ZK60 alloy had higher adhesive strength and better corrosion resistance than that on ME20 alloy. The coatings on ZK60 and ME20 alloys mainly had crystalline structures, and the coating on ME20 alloy had also a slight microcrystalline structure.

Key words: ZK60 magnesium alloys; ME20 alloys; electroless Ni plating; initial deposition; adhesive strength; corrosion resistance

1 Introduction

Magnesium (Mg) alloys afford advantages such as low density, high specific strength and specific stiffness, good biocompatibility, and good electromagnetic shielding. Therefore, they are widely used in a variety of applications that require lightweight structures, including the automotive, electronics, medical and health, and aerospace industries. However, Mg alloys have higher chemical activity and poorer corrosion resistance relative to aluminum alloys, which limit their applicability. Due to the increasing demand for Mg alloys, many studies on surface protection technologies have been conducted to improve the environmental adaptability of Mg alloys [1,2]. Mg alloys can be protected from corrosion through the formation of a surface coating using methods such as chemical conversion, electroplating, electroless plating, microarc oxidation, thermal spraying, laser surface treatment, chemical or physical vapor deposition, organic/polymer coating, and sol–gel coating. For a given engineering application, a suitable surface treatment method is selected according to the uses of the Mg alloy parts [3−6].

Compared with other technologies, electroless nickel (Ni) plating on Mg alloys has been extensively investigated because it affords excellent conductivity, corrosion resistance, and thickness uniformity, and is facile in terms of solution system and plating parameters such as the temperature and pH [7,8]. A nickel–phosphorus (Ni−P) composite coating on Mg alloys containing hard ceramic particles such as SiC, TiO_2, and Al_2O_3 has been developed to improve the corrosion and wear resistance [9,10]. However, performing uniform and dense electroless Ni plating on Mg alloys is

Corresponding author: Li FENG, Tel: +86-10-68115451, E-mail: nanxia1984@163.com
DOI: 10.1016/S1003-6326(21)65656-X

extremely difficult because Mg alloys have higher chemical activity in the plating solution and different phases with electrochemical heterogeneity in the substrate [11,12]. The deposition process of electroless Ni plating on Mg alloys is also highly complicated because of the replacement reaction between Ni and Mg in the initial stage of plating and the solution autocatalytic reaction [13−15]. Therefore, the surface state of the substrate directly affects the initial deposition behavior of the coating. For example, the AZ91D alloy coating preferentially grows with β-phase due to the electrical coupling between the β-phase and the eutectic α-phase [16,17]. The initial deposition of the coating on AZ31 alloy occurs preferentially at MgF_2 film defects because of the potential difference between α-phase and Mn−Al phase [18,19].

ZK60 and ME20 magnesium alloys possess high tensile strength and excellent welding performance, respectively, and are therefore widely used in aerospace electronic products. Electroless Ni−P coating is the main protection technology applied to these alloys. In the present study, the phase compositions of the substrates of ZK60 and ME20 alloys were investigated to clarify the initial deposition behavior during electroless Ni−P coating. Zn−Zr and Mg−Ce precipitates exist on ZK60 and ME20 alloy surfaces, respectively [20,21]. The number and activity of the Zr−Zn and Mg−Ce precipitates were found to affect the initial deposition mode and deposition rate of plating. The effects of the initial deposition on the corrosion resistance, microstructure, and adhesive strength of the coating were also investigated.

2 Experimental

2.1 Materials

Rolled sheets of ME20 and ZK60 alloys were used in this study. Table 1 lists the chemical compositions of these alloys. The specimen size was 10 mm × 10 mm × 2 mm, and the surface was mechanically polished with 2000-grit sandpaper and cleaned with deionized water.

2.2 Electroless Ni−P plating

Firstly, the specimens were pickled in a pickling solution comprising 20 mL/L H_3PO_4 (85%) and 10 mL/L HNO_3 (65%) for 20 s to roughen their surface to improve the adhesive strength between the coating and the substrate. Subsequently, they were activated in 150 mL/L HF (40%) for 2 min at room temperature. After these pretreatment steps were executed, the specimens were immediately transferred into the electroless plating solution containing 15 g/L $NiCO_3{\cdot}2Ni(OH)_2{\cdot}4H_2O$, 5 g/L $C_6H_8O_7{\cdot}H_2O$, 20 g/L $NaH_2PO_2{\cdot}H_2O$, 10 g/L NH_4HF_2, 12 mL/L HF (40%), and 1 mg/L $CS(NH_2)_2$ at 80 °C. The specimen was rinsed with distilled water at each step. Thereafter, the deposition rate, microstructure, adhesive strength, and corrosion resistance of the coating were compared.

To study the initial deposition behaviors of electroless Ni−P coating on ZK60 and ME20 alloys, the specimens were polished twice to a mirror surface (Fig. 1) and were corroded with specific solutions at room temperature for 20 s to obtain clear grain boundaries. ME20 alloy was corroded with $C_6H_8O_7{\cdot}H_2O$ solution (5 g/L) and ZK60 alloy, with a solution containing 1 mL/L HNO_3 (65%), 20 mL/L $C_2H_4O_2$, 60 mL/L $C_2H_6O_2$, and 19 mL/L H_2O. After HF activation, the specimens were immersed in the plating solution for different durations, namely, 20, 30, 40, 50, and 60 s. The evolution of the microstructure and elemental composition of different phases was characterized using scanning electron microscopy (SEM; ZEISS SUPER 55VP) with energy-dispersive spectroscopy (EDS).

2.3 Coating characterization

The deposition rate (v, μm/min) of the coatings was measured using the mass gain method and calculated as

$$v=10^4\Delta m/(\rho St) \quad (1)$$

where Δm (g) is the mass increment of the electroless Ni−P coating, ρ (g/cm^3) is the average density of the plating (Ni−P coating density: 8.1 g/cm^3), S (cm^2) is the surface area of the

Table 1 Chemical compositions of ME20 and ZK60 Mg alloys (wt.%)

Alloy	Mn	Zr	Ce	Al	Zn	Si	Fe	Cu	Be	Other	Mg
ME20	1.3−2.2	−	0.15−0.35	≤0.20	≤0.30	≤0.10	≤0.05	≤0.05	≤0.01	≤0.30	Bal.
ZK60	≤0.10	0.30−0.90	−	≤0.05	5.0−6.0	≤0.05	≤0.05	≤0.05	≤0.01	≤0.30	Bal.

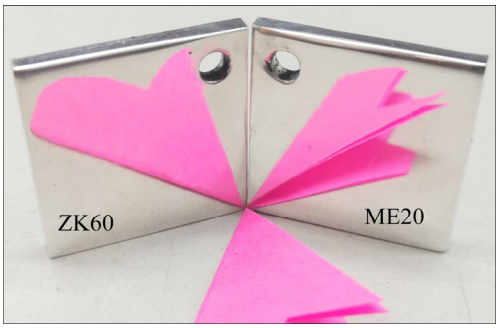

Fig. 1 Specimens after secondary mechanical polishing

specimen, and t (min) is the plating duration.

The microstructure and elemental composition of the coatings were analyzed using SEM and EDS. The crystal characteristics of the coatings were determined using X-ray diffractometry (XRD; DMAX−3B).

The adhesive strength of the coatings was evaluated using the thermal shock method. The process was repeated 30 times. The electroless Ni−P coating specimens were kept in a constant temperature oven at 200 °C for 1 h and then quickly placed into cold water. The specimens were removed from the water and dried using compressed air. Finally, the appearance of the specimens was checked.

The potentiodynamic polarization curve and potentiostatic polarization curve of the coatings were measured in 0.1 mol/L NaCl solution using an electrochemical workstation with a saturated calomel electrode as a reference electrode, platinum as a counter electrode, and specimens with an exposed area of 1 cm^2 as a working electrode.

3 Result and discussion

3.1 Microstructure of substrates

As shown in Fig. 2, clean grain boundaries of specimens were obtained through polishing and corrosion. As indicated in Fig. 2(a), a large number of precipitates were observed in the ZK60 alloy; these were mainly distributed near the grain boundaries, and their particle size was <2 μm. EDS linear scanning results of the precipitates indicated that their Mg content was significantly lower and their Zn and Zr contents were significantly higher (approximately 35 and 10 wt.%, respectively). The grains mainly comprised Mg and Zn (>5 wt.%) and only a small quantity of Zr (<1 wt.%). The inner grains and grain boundaries of the ZK60 alloy comprised Mg−Zn eutectic compounds (Mg_xZn_y) and a Mg-rich phase [22]. The precipitates were mainly Zn−Zr eutectic compounds, such as Zn_2Zr [23]. Fewer precipitates were observed in the ME20 alloy, and most of them were distributed at the grain boundaries and in the grains. EDS linear scanning maps of the precipitates indicated a

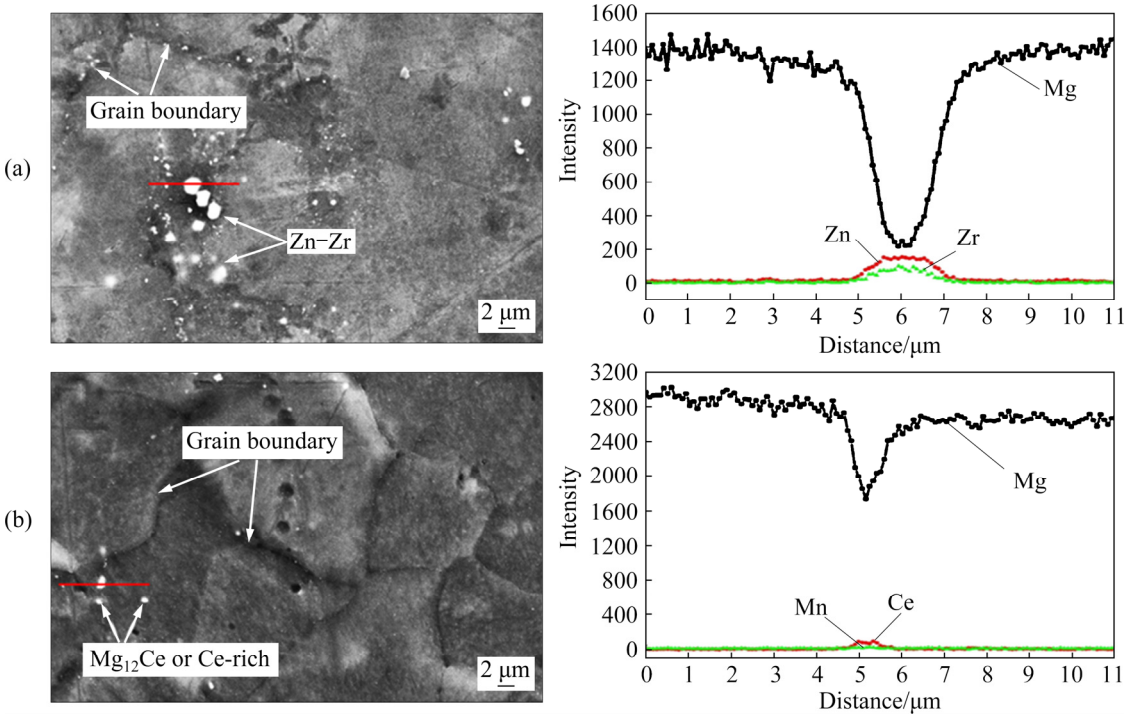

Fig. 2 Microstructures of substrate after corrosion and EDS linear scanning maps: (a) ZK60 alloy; (b) ME20 alloy

decreased Mg content and an increased Ce content. The inner grains and grain boundaries mainly comprised simple manganese and a Mg-rich phase. The precipitates were mainly $Mg_{12}Ce$ [24], and the Ce content of some larger precipitates (approximately 1 μm) exceeded 30 wt.%.

3.2 Initial deposition behavior

Figures 3 and 4 show the microstructures of ZK60 and ME20 alloys specimens, respectively, which were immersed in the plating solution for 0, 20, 30, 40, 50, and 60 s, respectively.

The precipitates on the surface of the ZK60 and ME20 alloys did not dissolve or degrade after HF activation. The F content of the corresponding precipitates was 1.4 and 7.9 wt.%, respectively (Zone I in Figs. 3(a) and 4(a)); however, the F content of the grains was approximately 1.5 wt.% (Zone II in Figs. 3(a) and 4(a)). The Mg in the precipitates and grains reacted with HF to form MgF_2 (Reaction 2) that could prevent the corrosion of the magnesium alloy in the plating solution and that controlled the initial deposition rate [25,26]. The other three constituents Zn, Zr, and Ce of the precipitates probably reacted with HF to form ZnF_2, ZrF_4, and CeF_4, respectively (Reaction 3).

The difference in F content between the two precipitates was related to the solubility of fluoride. ZnF_2 and ZrF_4 are slightly soluble in water, whereas MgF_2 and CeF_3 are insoluble in water.

$$Mg+2HF\rightarrow MgF_2+H_2\uparrow \quad (2)$$

$$M(Zn,Zr,Ce)+HF\rightarrow MF_x+H_2\uparrow \quad (3)$$

The EDS analysis revealed that Ni and P were absent on the surface of the ZK60 and ME20 alloys after these specimens were immersed in the plating solution for 20 s (Figs. 3(b) and 4(b)). After 30 s, the morphology of the grains and grain boundaries was not significantly changed for both ZK60 and ME20 alloys (Zone II in Figs. 3(c) and 4(c)). MgF_2

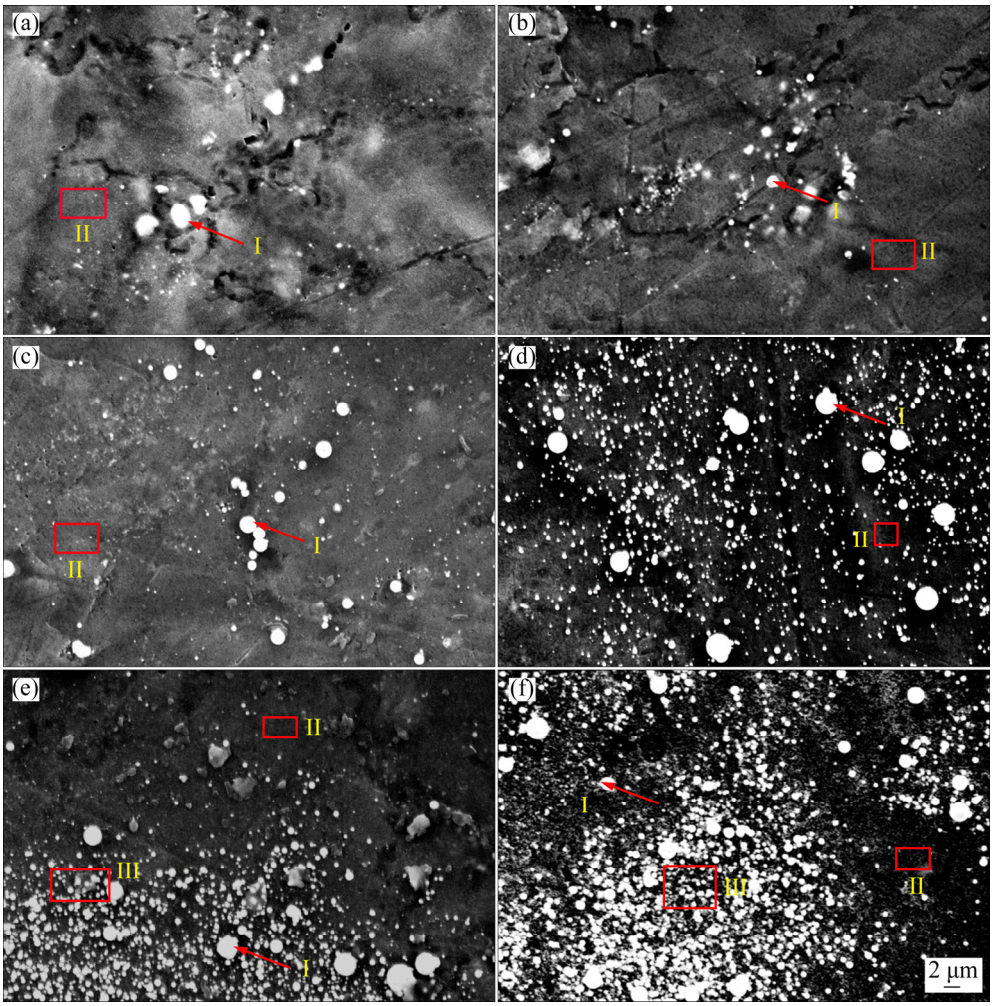

Fig. 3 Microstructures of ZK60 alloy specimen after plating for 0 s (HF activation) (a), 20 s (b), 30 s (c), 40 s (d), 50 s (e), and 60 s (f)

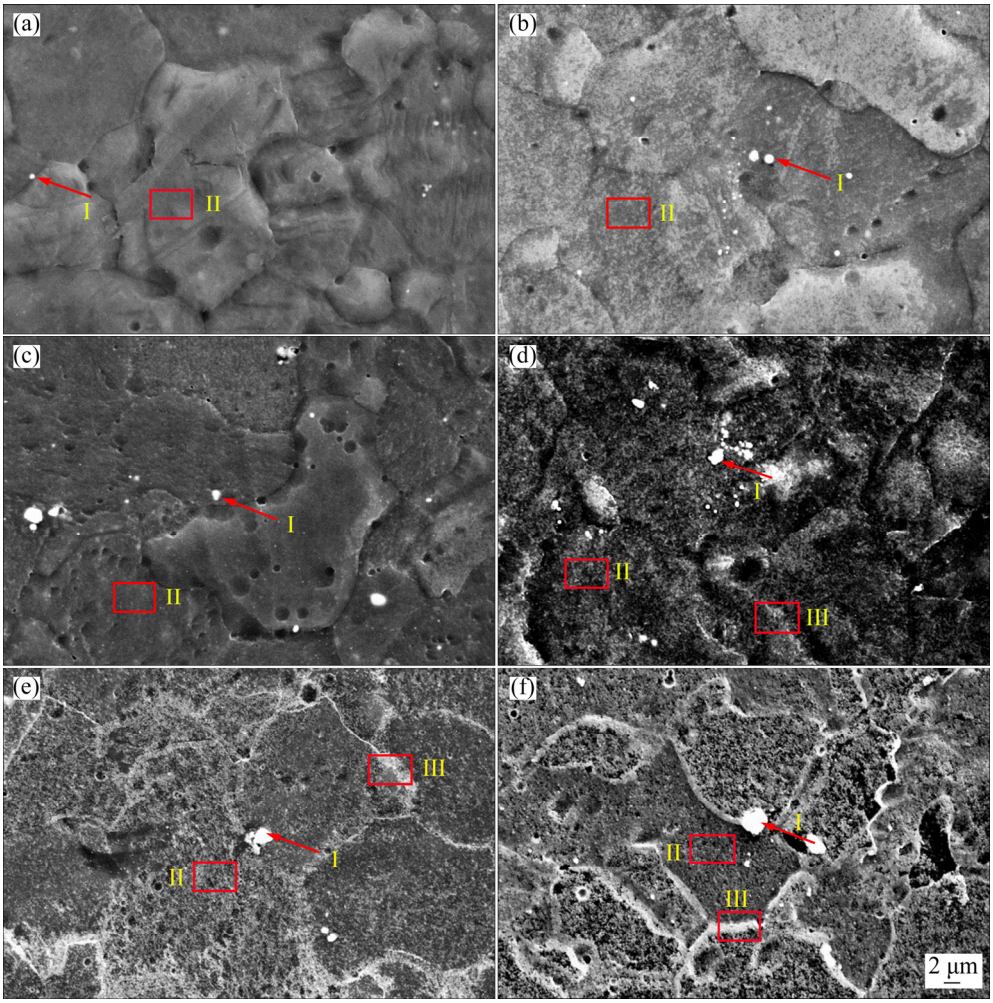

Fig. 4 Microstructures of ME20 alloy specimen after plating for 0 s (HF activation) (a), 20 s (b), 30 s (c), 40 s (d), 50 s (e), and 60 s (f)

film was formed on the alloy surface after HF activation. This film could prevent the solution from contacting the substrate, the substitution reaction between Ni and Mg and the solution autocatalytic reaction.

However, Ni and P were detected on the precipitates (Zone I in Figs. 3(c) and 4(c)). The Ni and P contents of the precipitates in ZK60 alloy were 53.63 and 9.04 wt.%, respectively, and those in ME20 alloys were 41.09 and 2.39 wt.%, respectively (Tables 2 and 3); the content difference was mainly caused by the elements constituting the precipitates. The detection of P indicated that the solution autocatalytic reaction occurred on the precipitates. For the ZK60 alloy, few fluorides were detected on the precipitates. Fluorides could not form a continuous and dense film on the precipitates of ME20 alloy due to the presence of Ce. Consequently, the precipitates possessed higher chemical activity than the grains. The elements in the precipitates were preferentially replaced with Ni ions in the solution to form Ni catalytic active sites (Reaction 4), thereby undergoing a solution autocatalytic reaction:

$$N(Mg,Zn,Zr,Ce)+Ni^{2+}\rightarrow Ni+N^{x+}(Mg^{2+}, Zn^{2+}, Zr^{4+}, Ce^{4+}) \quad (4)$$

Meanwhile, the P and Ni contents of the precipitates in ZK60 alloy were higher than those of the precipitates in ME20 alloy, indicating that the precipitates in ZK60 alloy possessed higher chemical activity. For the ZK60 alloy, the main component of the precipitates was Zn−Zr eutectic compounds. After HF activation, Zn and Zr were dissolved in the solution as fluorides, and only a small quantity of MgF_2 remained in the precipitates. Therefore, the element could be rapidly replaced by Ni ions to form catalytic active sites. By contrast, in ME20 alloy, the main component of the precipitates was $Mg_{12}Ce$. During HF activation, the fluorides

Table 2 Contents of main elements in ZK60 alloy for different plating time (wt.%)

Time/s	Zone code	F	Mg	Zn	Zr	Ni	P
0	I	1.38	53.71	34.87	9.42	−	−
	II	1.53	90.42	7.01	1.04	−	−
20	I	0.71	64.16	28.07	5.60	−	−
	II	1.13	89.37	6.96	−	−	−
30	I	−	15.52	1.21	−	53.63	9.04
	II	1.22	87.88	7.53	1.20	−	−
40	I	−	7.80	1.53	−	80.70	9.09
	II	1.36	89.16	6.04	0.84	−	−
50	I	−	5.29	1.52	−	80.96	9.88
	II	2.53	86.27	6.82	−	0.68	0.45
	III	2.21	81.61	7.05	−	4.79	0.92
60	I	−	15.39	1.12	−	74.60	7.11
	II	3.17	84.41	5.52	−	3.28	0.64
	III	3.27	72.48	5.68	−	14.37	1.72

Table 3 Contents of main elements in ME20 alloy for different plating time (wt.%)

Time/s	Zone code	F	Mg	Mn	Ce	Ni	P
0	I	7.93	67.65	−	20.08	−	−
	II	1.53	96.19	1.25	−	−	−
20	I	5.46	72.24	−	20.17	−	−
	II	2.06	93.47	1.43	−	−	−
30	I	4.38	45.64	−	6.50	41.09	2.39
	II	1.49	96.91	1.61	−	−	−
40	I	4.84	30.92	−	4.84	55.05	2.91
	II	1.04	95.93	1.64	−	−	−
	III	2.09	95.26	1.23	−	2.49	1.02
50	I	2.24	28.29	−	2.72	60.95	3.92
	II	2.10	91.10	1.51	−	2.53	0.40
	III	2.59	86.45	1.24	−	6.85	1.09
60	I	2.46	17.33	−	2.56	70.72	5.34
	II	3.76	71.23	1.42	−	18.75	2.69
	III	2.18	59.75	0.91	−	30.72	4.15

formed by Mg and Ce remained in the precipitates because they were insoluble in the solution, and this reduced the displacement reaction rate.

After immersion for 40 s, a large number of precipitates in ZK60 alloy were observed (Fig. 3(d)); these could be divided into two types. One type was exposed on the top surface of the substrate. The other type was embedded in the substrate and was enveloped by the MgF_2 film; therefore, it could not react with the solution. MgF_2 film near the precipitate was loose, and cracks were even formed in MgF_2 film as its thickness increased [27,28]. As the immersion time increased, the Ni ions in the solution gradually passed through MgF_2 film and reacted with the precipitates. However, MgF_2 film on the grains was compact, thereby preventing Ni ions from migrating to the substrate; therefore, Ni and P were not detected on the grain surface (Zone II in Fig. 3(d)). For the ME20 alloy, the microroughness of the grains and grain boundaries increased significantly (Fig. 4(d)). Ni and P were detected at the grain boundaries but not on the grains. This is because MgF_2 film at the grain boundaries was looser than that on the surface of grains owing to surface defects [29], and Ni ions could easily migrate to the substrate. In short, the substitution reaction between Ni ions and Mg occurred preferentially at the grain boundaries.

As the immersion time increased, the size and quantity of precipitates on the surface of ZK60 alloy gradually increased (Zone I in Figs. 3(e) and (f)), and small amount of Ni and P were detected on the grains (Zone II in Figs. 3(e) and (f), and Table 2). The Ni content in the dense area of the precipitates (Zone III in Figs. 3(e) and (f)) was much higher than that on the grains. This was probably because the coating initially deposited on the precipitates. As the autocatalytic reaction progressed, the coating grew into round precipitates and expanded in two dimensions, and the MgF_2 film around the precipitates was torn by coating growth. Consequently, the compactness of the MgF_2 film decreased and the autocatalytic reaction around the precipitates was promoted.

For the ME20 alloy, after being immersed in the plating solution for 50 or 60 s, the grain boundary contour became clearer due to the increased Ni and P contents (Figs. 4(e) and (f)). Ni and P were also detected on the surface of grains, indicating that the autocatalytic reaction occurred. Compared with the grain and grain boundary after immersion for 40, 50, and 60 s, the Ni and P contents at the grain boundaries were much higher than those on grains mainly owing to the higher chemical activity at grain boundaries.

The MgF_2 film was porous and contained MgO (or $Mg(OH)_2$) [30,31]. The Ni ions in the plating solution could react with the substrate through the pores or the defects formed by the dissolution of MgO (or $Mg(OH)_2$). Under the same HF activation conditions, the compactness of the MgF_2 film was related to the elemental composition of substrates [27,32]. Further, the compactness of the MgF_2 film determined the deposition rate of the coating. After 50 and 60 s, the Ni content of the grains in ZK60 alloy was 0.68 and 3.28 wt.%, respectively, and that of the grains in ME20 alloy was 2.53 and 18.75 wt.%, respectively. To compare the MgF_2 film of ZK60 and ME20 alloys, potentiodynamic polarization curves of specimens with and without HF activation were obtained (Fig. 5). The corrosion potentials of the ZK60 alloy with and without HF activation were −1.36 and −1.23 V, respectively, and those of the ME20 alloy were −1.31 and −1.28 V, respectively. The difference in corrosion potential indicated that the compactness of the MgF_2 film on ZK60 was better than that on ME20. For the ME20 alloy, a large quantity of simple manganese dispersed on the surface and reduced the compactness of the MgF_2 film. However, for the ZK60 alloy, Zn and Mg in the grains existed as eutectic compounds that had no influence on the compactness of the MgF_2 film. After HF activation, the MgF_2 film on the ZK60 alloy could improve the corrosion resistance of the substrate. Owing to the higher density of the MgF_2 film on the grains of the ZK60 alloy, fewer dissolution defects were formed. Consequently, the Ni and P contents of grains were lower during the same period.

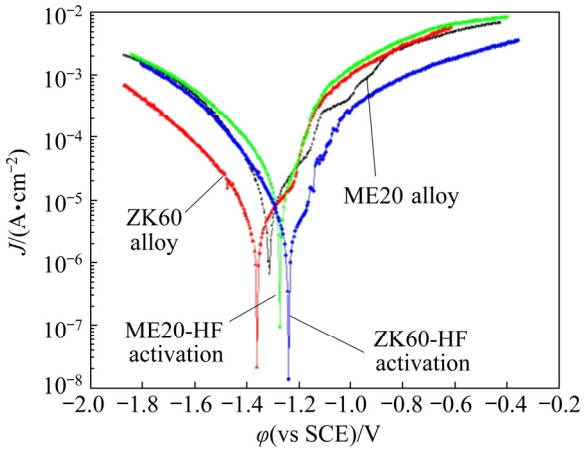

Fig. 5 Dynamic potential polarization curves of substrates before and after HF activation

The deposition process indicated that, in the early stage of electroless Ni–P coating, the deposition rate of ZK60 was controlled by precipitates, whereas that of ME20 was controlled by the MgF_2 film.

Figure 6(a) shows the initial deposition process of electroless Ni−P coating on the ZK60 alloy. Three findings were obtained. Firstly, after the substrate was corroded, a large number of precipitates were exposed on the surface. Owing to the formation of soluble fluoride on the precipitates after HF activation, the quantity of fluoride was small. Therefore, the precipitates had higher chemical activity relative to the grains and grain boundaries, and the initial deposition of the coating preferentially occurred on the bare precipitates, especially on larger ones. Secondly, as the immersion time increased, the precipitates embedded in the substrate and enveloped by the MgF_2 film came into contact with the solution; subsequently, the replacement and solution autocatalytic reactions occurred, resulting in the tearing of the MgF_2 film around the precipitates. Thirdly, the coating surrounded the precipitates in the early stage of growth and then expanded in two and three dimensions through the solution autocatalytic reactions. At the same time, the replacement reactions or autocatalytic reactions occurred on the grains and at grain boundaries.

The electroless Ni−P coating deposition process significantly differed between ME20 and ZK60 alloys. Insoluble fluoride was formed on the precipitates after HF activation; however, the replacement reaction could not be prevented because of the poorer density relative to that of the grains. Therefore, the coating was preferentially deposited on the precipitates. However, the growth trend of the coating was not affected due to the small quantity of precipitates. In addition, the porosity of the MgF_2 film on ME20 alloy was higher, and more soluble (MgO (or $Mg(OH)_2$)) defects were observed due to the presence of simple manganese. Therefore, the substitution reaction easily occurred on the grains or at grain boundaries of the ME20 alloy. However, the coating growth was mainly related to the compactness of the MgF_2 film in different regions of the substrate, as shown in Fig. 6(b). The MgF_2 film on the grains was denser than that at grain boundaries, and, therefore, the replacement reaction between Ni ions and Mg

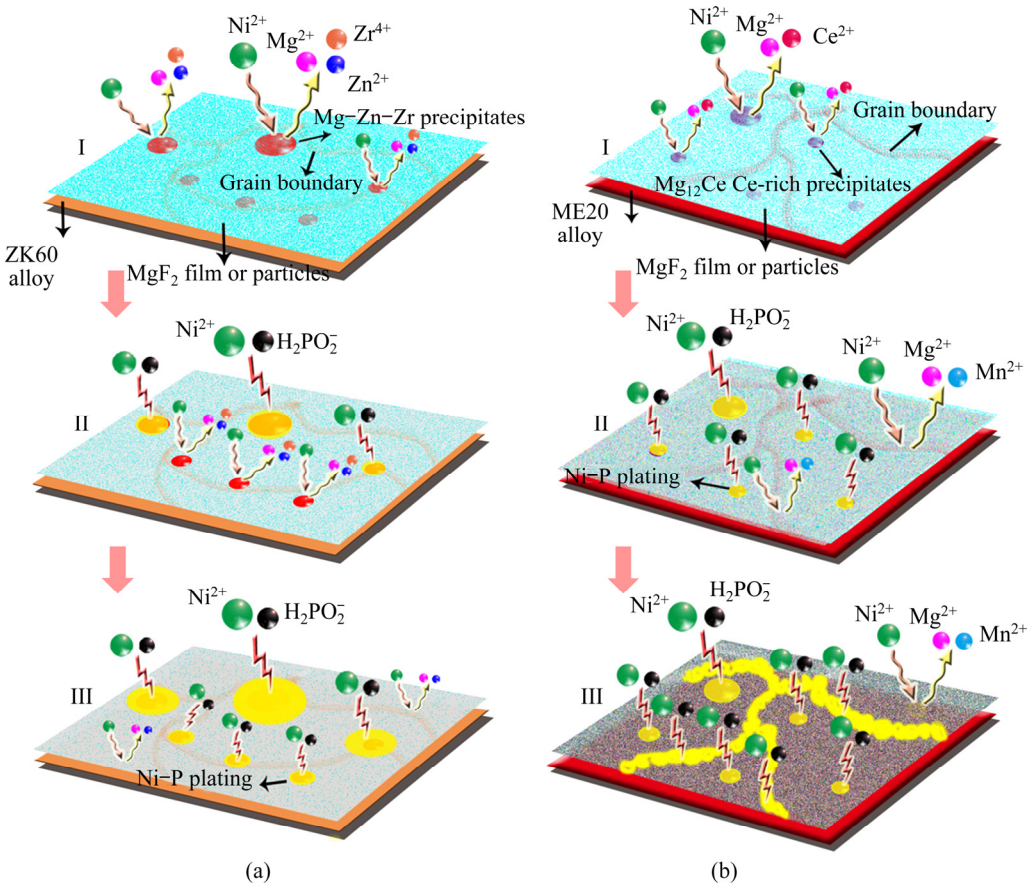

Fig. 6 Initial deposition process of electroless Ni−P coating on ZK60 (a) and ME20 (b) alloys

occurred firstly at the grain boundaries and then on the grains. As the immersion time increased, Ni catalytic active sites were formed on the substrate, and the coating gradually covered the whole substrate.

3.3 Deposition rate

Figure 7 illustrates the mass increment and plating deposition rate of the same specimens at different time. At the initial stage, the mass increment and plating deposition rate of the ZK60 alloy were much higher than those of the ME20 alloy. The difference in deposition rate was related to the initial deposition process. At the initial deposition stage of coating on the ZK60 alloy, the solution autocatalytic reaction mainly occurred around the precipitates, and large number of precipitates on the substrate could form more catalytic active centers. Therefore, the two-dimensional deposition rate was accelerated at the early stage.

The initial deposition of the plating on the ME20 alloy also occurred on precipitates; however, the precipitates did not influence the deposition rate due to their small quantity and low activity. The initial catalytic active sites on ME20 alloy were mainly formed by the replacement reaction of Ni ions with Mg. The migration rate of Ni ions was low due to the shielding of the MgF_2 film, and this further affected the replacement reaction rate. Consequently, the compactness of the MgF_2 film on ME20 alloy determined the initial deposition rate.

After 5 min, the plating deposition rate of ZK60 alloy decreased, whereas that of ME20 alloy continued to increase. Figure 8 displays the microstructures of the coatings after 5 and 15 min. After 5 min, the Mg contents on the substrate of the ZK60 and ME20 alloys were 2.18 and 16.68 wt.%, respectively (Figs. 8(a) and (b)). The substrate of the ZK60 alloy was completely covered by the coating, and the solution autocatalytic reaction mainly occurred on the surface. However, the coating on the ME20 alloy did not completely cover the substrate. The solution autocatalytic reaction and replacement reaction were suggested to occur simultaneously on the surface. Ni catalytic active

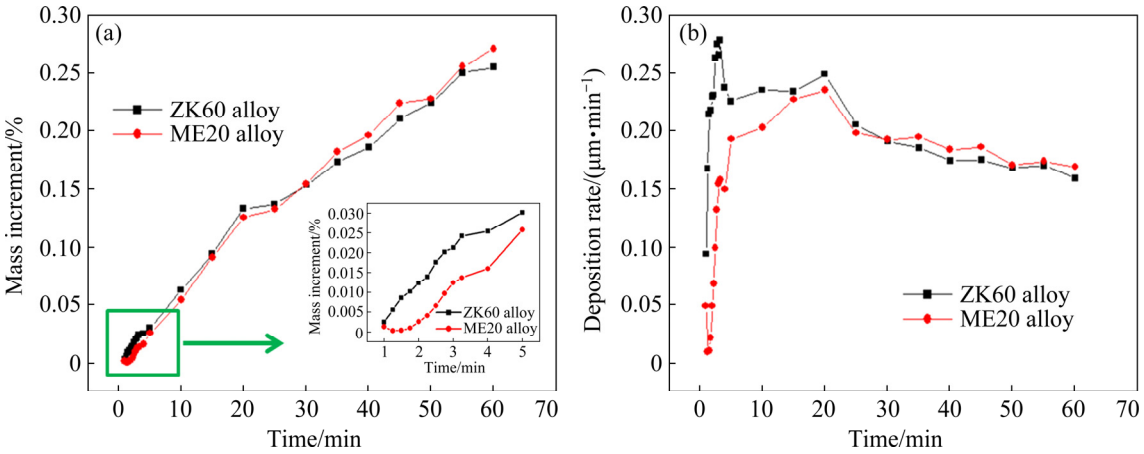

Fig. 7 Mass increment (a) and plating deposition rate (b) of specimens at different plating time

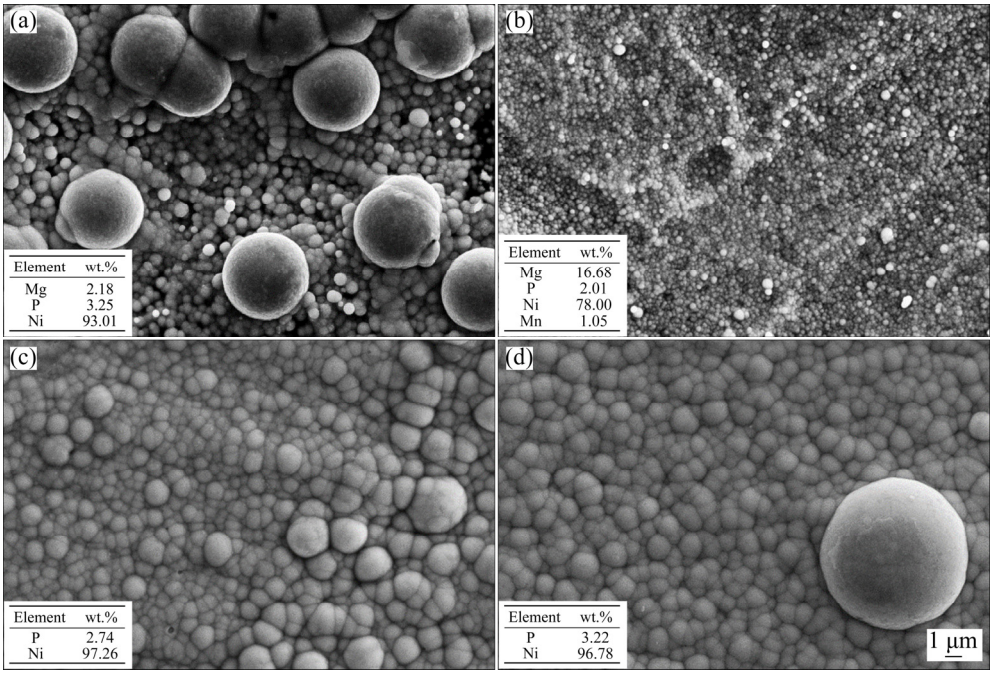

Fig. 8 Microstructures with electroless Ni plating for different time: (a) ZK60 alloy, 5 min; (b) ME20 alloy, 5 min; (c) ZK60 alloy, 15 min; (d) ME20 alloy, 15 min

sites and the early Ni–P coating with smaller nodules had high catalytic activity. With the growth of the coating, the microstructure of the coating, including the size and number of nodules, tended to be consistent (Figs. 8(c) and (d)). The deposition rates between the two magnesium alloys did not differ significantly. As the compactness of the coating increased, the surface activity decreased and deposition rate tended to decrease.

3.4 Microstructure

Figure 9 shows the microstructures of magnesium alloys after electroless Ni–P coating for 30, 45, and 60 min. For ZK60 and ME20 alloys, the nodule size of the coating increased with increasing the plating time, but the microstructure of the coating did not. Figure 8 shows that after 15 min, the substrates were completely covered by the coating and that the microstructures of the coatings were consistent. Subsequent coating growth was mainly achieved through the solution auto-catalytic reaction. The microstructural changes were dependent on the solution system rather than on the initial deposition method. However, under the same conditions, the P content in the coating on the ME20 alloy was slightly higher than that in the coating on the ZK60 alloy; this may be related to the slightly faster deposition rate of the coating on

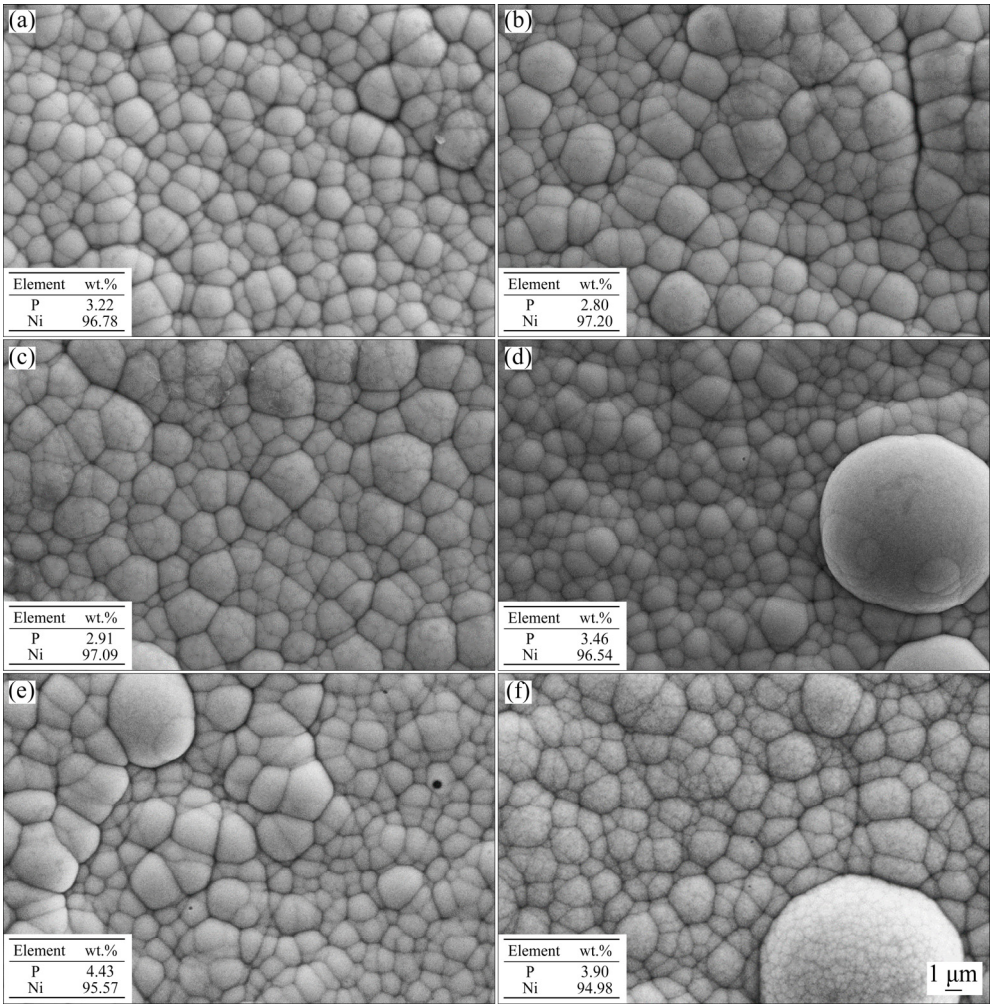

Fig. 9 Microstructures with electroless Ni plating for different time: (a) ZK60 alloy, 30 min; (b) ZK60 alloy, 45 min; (c) ZK60 alloy, 60 min; (d) ME20 alloy, 30 min; (e) ME20 alloy, 45 min; (f) ME20 alloy, 60 min

the ME20 alloy at the end of plating.

The crystal structure of the electroless Ni–P coating depends on the P content. Generally, coatings with low, intermediate, and high P contents (≤3%, 3%−6%, and ≥9%, respectively) have crystalline, amorphous, and microcrystalline structures, respectively [33]. Figure 10 shows XRD patterns of the Ni–P coating on these two Mg alloys; no significant differences were seen in the number and position of the diffraction peaks. The diffraction peaks near 2θ value of 45° corresponded to the Ni (111) plane. The Mg (100), (002), (101), and (103) diffraction peaks in the XRD profiles were attributable to the substrate of Mg alloys. This was probably because X-ray penetrated the thin coating (12−13 μm in 60 min) to the substrate [34]. The full width at half maximum values of the Ni characteristic peak of the coating (60 min) on ZK60 and ME20 alloys were 0.866 and 0.887, respectively, indicating that the coating on the ZK60 alloy was more crystalline. This result was consistent with the EDS result. The coatings on the two Mg alloys were mainly crystalline, and a small amount of microcrystalline structure was mixed in the coating on the ME20 alloy.

3.5 Adhesive strength

The thermal shock test can be used to determine the adhesive strength of the coating when the thermal expansion coefficients of the coating and the substrate are not identical. The thermal expansion coefficients of the electroless Ni plating and Mg alloy were approximately 13×10^{-6} and 22×10^{-6} °C^{-1}, respectively. After the thermal shock test, the coating on the ME20 alloy peeled and cracked whereas that on the ZK60 alloy almost

remained, indicating higher bonding strength of the ZK60 alloy (Fig. 11). When the Ni−P coating and Mg alloy were rapidly cooled from a high to a low temperature, their respective deformations differed greatly. If the intrinsic stress of the coating was large, peeling and cracking were likely to occur [35]. The intrinsic stress of the coating was caused by lattice defects or lattice growth defects during deposition and was closely related to the electroless Ni plating solution system and the plating parameters [36,37]. The adhesive strength of the metal plating and the substrate mainly depended on the metal bonding and mechanical joint, which was roughened by pickling or sandblasting [38−40]. After pickling and activation, the microroughness of the substrates on the ZK60 and ME20 alloys did not differ significantly. After 60 min, the P content, microstructure, and thickness of the coating on the ME20 alloy were approximately the same as those of the coating on the ZK60 alloy. However, the coating on the ME20 alloy peeled and cracked, indicating that it had a larger intrinsic stress. Because the plating conditions of ZK60 and ME20 alloys were the same, the difference in intrinsic stress was closely associated with the initial deposition behavior of the coating.

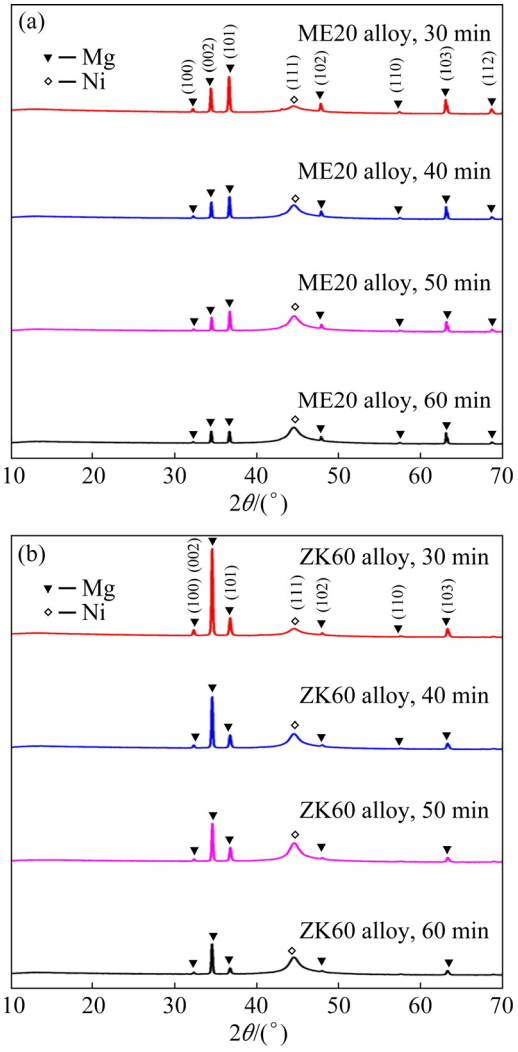

Fig. 10 XRD patterns of Ni−P coating for different plating time: (a) ME20 alloy; (b) ZK60 alloy

Fig. 11 State of plating after thermal shock test

The coating was peeled off from the substrate using a surgical blade. SEM was used to analyze the stripped plating (i.e., contact surface with substrate) and stripped area (Fig. 12). The nodules of the stripped plating on ZK60 alloy exhibited obvious divisions between each other. However, the nodules of the stripped plating on ME20 alloy were stuck together. This indicated that the initially deposited plating on ZK60 alloy had a smaller internal stress. The difference in microstructure was closely related to the initial deposition method. When the coating on ZK60 alloy was peeled off, a large quantity of precipitates were exposed on the substrate. These precipitates contained Mg (57.34 wt.%), P (3.11 wt.%), Ni (34.64 wt.%), and Zn (2.20 wt.%), indicating that they were Zn−Zr eutectic compounds covered with Ni−P coating. The nonprecipitate region contained Mg (91.82 wt.%), Zn (7.48 wt.%), and Zr (0.70 wt.%), and Ni and P were not detected. This further illustrated that the initially deposited coating on the ZK60 alloy mainly surrounded the precipitates and expanded in two dimensions through the solution autocatalytic reaction. A large number of precipitates achieved independent deposition of the coating, and these could further reduce the internal stress of the coating. The initial Ni–P coating was combined with precipitates through metal–metal bonds. The precipitates exhibited excellent adhesive strength with the substrate and connected the coating with the substrate-like rivets. Therefore, the coating on the ZK60 alloy had excellent adhesive strength.

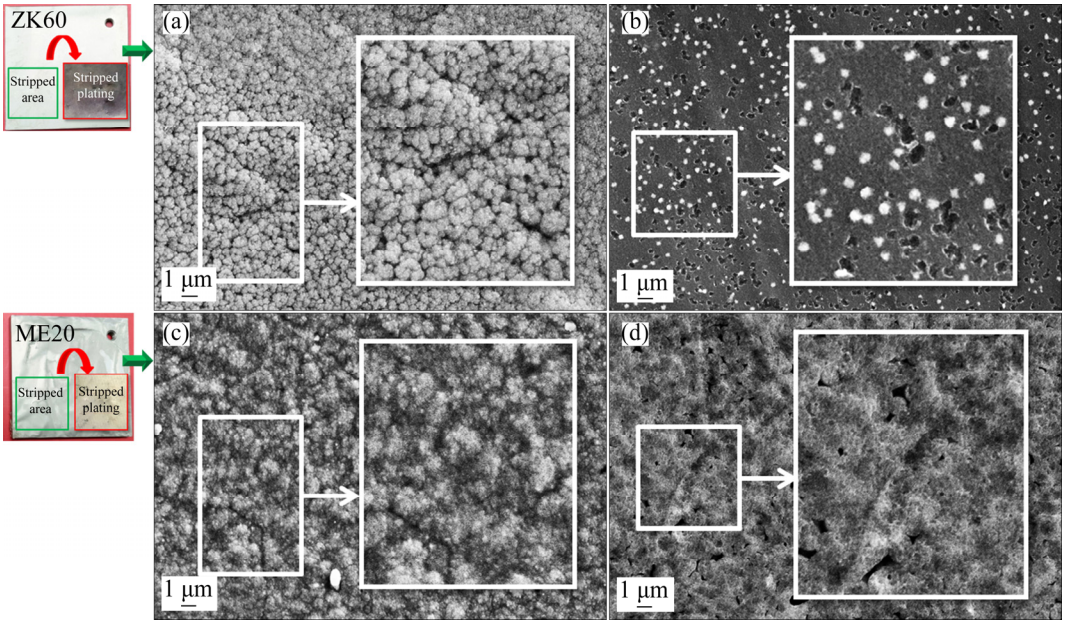

Fig. 12 SEM images showing microstructure of stripped plating (a, c) and stripped area (b, d)

When the coating on the ME20 alloy was peeled off, the exposed surface mainly contained F (5.84 wt.%), Mg (14.17 wt.%), P (9.37 wt.%), and Ni (66.9 wt.%). This demonstrated that the initially deposited plating remained on the substrate and was mixed with MgF_2. A large number of Ni catalytic active sites were formed during the initial deposition stage, and these promoted the solution autocatalytic reaction, especially the reduction reaction of $Na_2H_2PO_2$. Consequently, the P content was higher in the initially deposited plating. Because the P content of the stripped plating was low (approximately 4 wt.%), the crystal structures of the initial and final coatings differed. Ni could bond with the substrate through a metal–metal bond, and the initially deposited coating obtained through Ni active site catalysis had higher adhesive strength with the substrate. The stripped plating grew on the initial coating. Due to the mismatch of the crystal structure between the initial Ni−P coating and the stripped plating and the presence of MgF_2, the adhesive strength of the coating was reduced.

3.6 Corrosion resistance

Figure 13 displays the potentiodynamic polarization curves of the Ni−P coating after plating for 10, 20, 30, 40, 50, and 60 min. The polarization curves were analyzed using the cathodic Tafel extrapolation technique [41]. Table 4 lists the corrosion current density (J_{corr}) and corrosion potential (φ_{corr}). It indicated that the corrosion potential of the coating increased and the corrosion current density decreased as the plating time increased, indicating that the corrosion resistance of the coating exhibited an upward trend. In addition, the corrosion potential of the Ni–P coating on ZK60 alloy was higher than that of the same coating on ME20 alloy, indicating that the former coating had higher corrosion resistance. Figure 14 displays the potentiostatic polarization curves of the coating for different time. Figure 14(a) indicated that the corrosion of the coating on ME20 and ZK60 alloys for 40 min occurred at approximately 15 and 25 min, respectively. The coating on ME20 alloy for 60 min exhibited corrosion at approximately 20 min, whereas that on the ZK60 alloy for 60 min did not exhibit corrosion (Fig. 14(b)). This result further demonstrated that the Ni−P coating on ZK60 had better protection capability.

During electroless Ni plating, closed or open holes appeared on the coating surface due to the release of hydrogen [42]. The resulting open pores affected the corrosion resistance. The difference in open pores in the coating on the ZK60 and ME20 alloys was closely related to the initial deposition behavior. After the Ni−P coating was peeled from the substrate, numerous pit defects were observed on the surface of the ZK60 alloy (Fig. 15(a)). An EDS analysis revealed that the pit defects mainly contained Mg and Zn. These pit defects were formed by the peeling of precipitates with the coating. As shown in Fig. 15(b), microhole defects

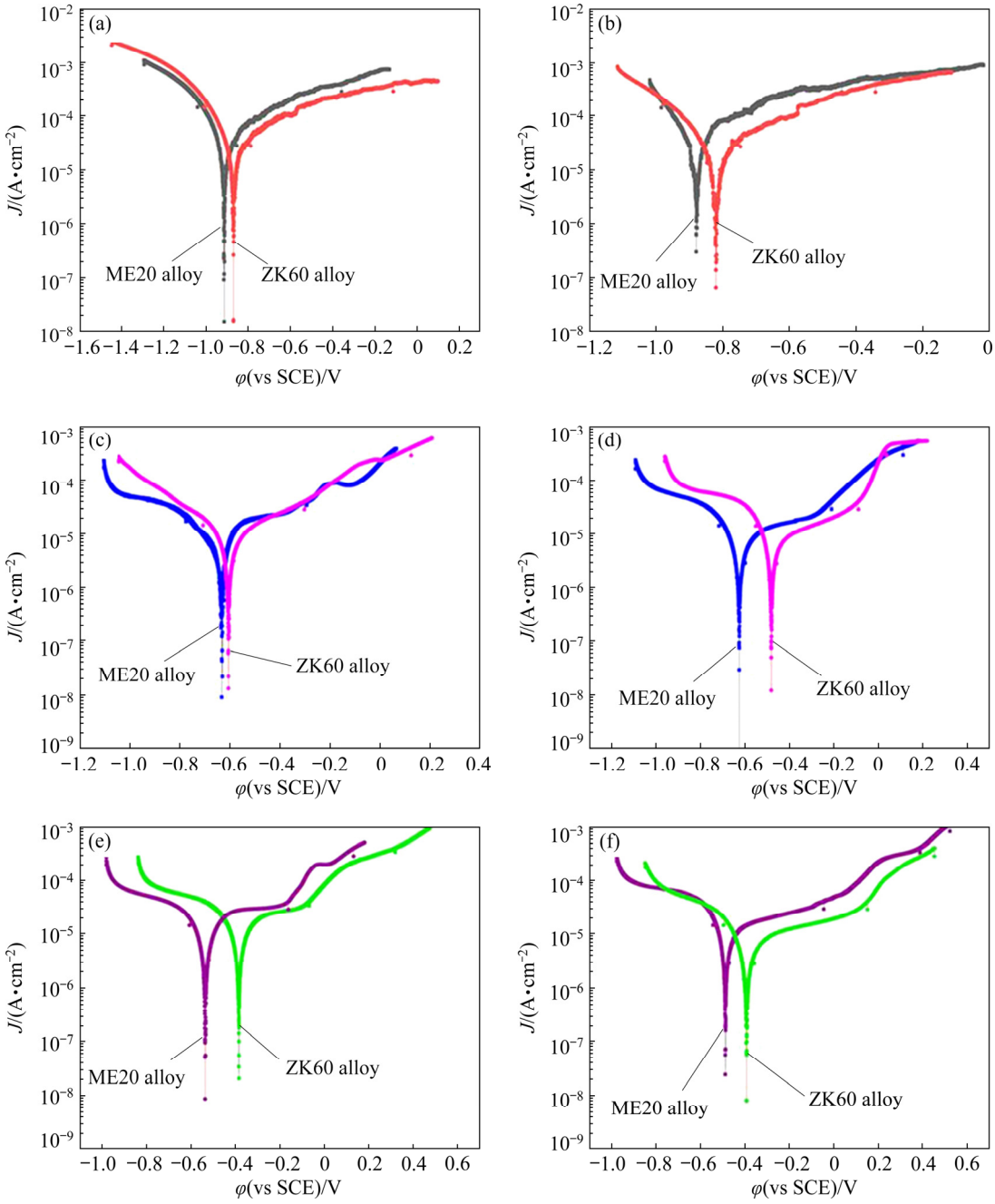

Fig. 13 Dynamic potential polarization curves of Ni−P coating after plating for different time: (a) 10 min; (b) 20 min; (c) 30 min; (d) 40 min; (e) 50 min; (f) 60 min

Table 4 Corrosion potential and corrosion current density of Ni−P coating after plating for different time

Time/min	φ_{corr}(vs SCE)/V		$J_{corr}/(10^{-5}A\cdot cm^{-2})$	
	ME20	ZK60	ME20	ZK60
10	−0.91	−0.86	2.51	1.63
20	−0.87	−0.82	1.67	1.35
30	−0.63	−0.60	0.74	0.68
40	−0.62	−0.48	0.65	0.49
50	−0.53	−0.39	0.56	0.46
60	−0.48	−0.39	0.54	0.37

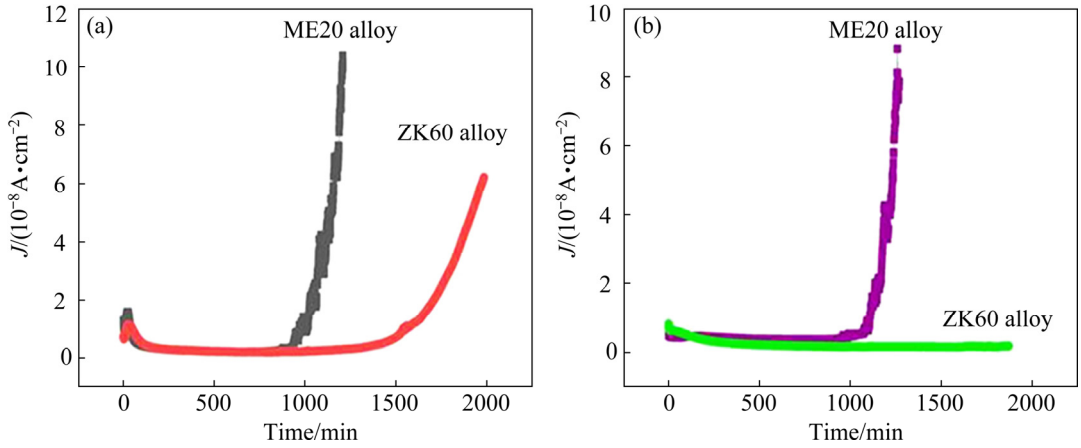

Fig. 14 Potentiostatic polarization curves of Ni−P coating after plating for 40 min (a) and 60 min (b)

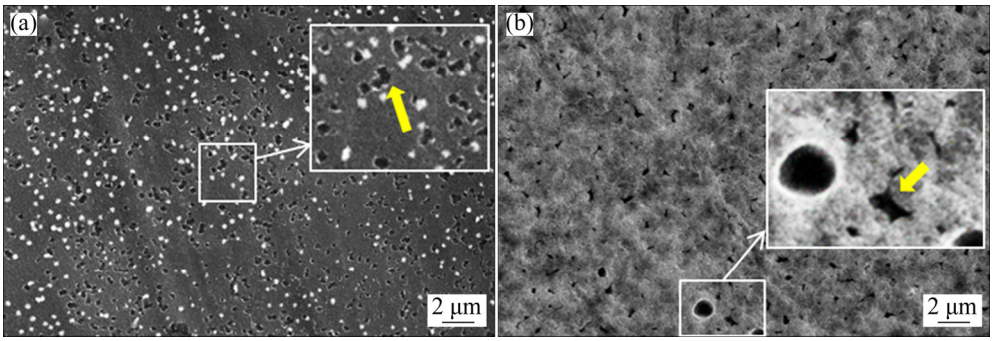

Fig. 15 Microstructures of substrate after coating being peeled off: (a) ZK60 alloy; (b) ME20 alloy

on ME20 alloy comprised Mg and F rather than Ni and P. These defects were supposed to be the denser MgF_2 film that could prevent the formation of Ni catalytic active sites. These defects did not possess catalytic activity and could only be covered by the Ni−P coating in two or three dimensions; this increased the probability of open pores and thereby affected the corrosion resistance of the coating. Consequently, the Ni−P coating on the ZK60 alloy had better continuity and higher corrosion resistance relative to the coating on the ME20 alloy.

4 Conclusions

(1) The initial deposition of the coating on ZK60 alloy occurred preferentially on highly active Zn−Zr precipitates and then expanded in two dimensions through the solution autocatalytic reaction. The Mg−Ce precipitates on ME20 alloy did not affect the initial deposition rate of the coating due to their lower activity. The initial deposition of the coating on ME20 alloy was mainly controlled by the compactness of the MgF_2 film.

(2) The precipitates on ZK60 alloy reduced the internal stress of the initially deposited coating. This contributed to the excellent adhesive strength of the Ni−P coating with the substrate. The crystal structure of the initial Ni−P coating with high P content and the final coating on the ME20 alloy did not match. Meanwhile, the MgF_2 film was mixed in the initially deposited coating. Consequently, the adhesive strength of the Ni−P coating on ME20 alloy was lower.

(3) The morphologies of the coatings on ME20 and ZK60 alloys did not differ significantly. However, the probability of pores in the coating on ME20 alloy was higher. Consequently, the Ni–P coating on ZK60 alloy was denser than that on ME20 alloy, and the former exhibited excellent corrosion resistance.

References

[1] ATRENS A J, SONG G L, LIU M, SHI Z, CAO F, DARGUSCH M S. Review of recent developments in the field of magnesium corrosion [J]. Advanced Engineering Materials, 2015, 17(4): 400−453.

[2] LIU Yong, REN Hui, HU Wen-cheng, LI De-jiang, ZENG Xiao-qin, WANG Ke-gang, LU Jian. First-principles calculations of strengthening compounds in magnesium alloy: A general review [J]. Journal of Materials Science and Technology, 2016, 32: 1222−1231.

[3] NEZAMDOUST S, SEIFZADEH D, RAJABALIZADEH Z. Application of novel sol−gel composites on magnesium alloy [J]. Journal of Magnesium and Alloys, 2019, 7: 419−432.

[4] FERNANDEZ-HERNAN J P, LOPEZ A J, TORRES B, RAMS J. Silicon oxide multilayer coatings doped with carbon nanotubes and graphene nanoplatelets for corrosion protection of AZ31B magnesium alloy [J]. Progress in Organic Coating, 2020, 148: 105836.

[5] SAMADIANFARD R, SEIFZADEH D, HABIBI-YANGJEH A, JAFARI-TARZANAHG Y. Oxidized fullerene/sol−gel nanocomposite for corrosion protection of AM60B magnesium alloy [J]. Surface and Coatings Technology, 2020, 385: 125400.

[6] ZHANG Wan-neng, WANG Lin-zhi, FENG Zhong-xue, CHEN Yu-ming. Research progress on selective laser melting (SLM) of magnesium alloys: A review [J]. Optik, 2020, 10: 163842.

[7] HU Rong, SU Yong-yao, LIU Hong-dong. Deposition behaviour of nickel phosphorus coating on magnesium alloy in a weak corrosive electroless nickel plating bath [J]. Journal of Alloys and Compounds, 2016, 658: 555−560.

[8] RAJABALIZADEH Z, SEIFZADEH D. Application of electroless Ni−P coating on magnesium alloy via CrO_3 /HF free titanate pretreatment [J]. Applied Surface Science, 2017, 422: 696−709.

[9] GHAVIDEL N, ALLAHKARAM S R, NADERI R, BARZEGAR M. Corrosion and wear behavior of an electroless Ni−P/nano-SiC coating on AZ31 Mg alloy obtained through environmentally-friendly conversion coating [J]. Surface and Coatings Technology, 2020, 382: 125156.

[10] CARRILLO D F, BERMUDEZ A, GOMEZ M A, ZULETA A A. Fretting-corrosion behavior of electroless Ni−P/Ni−P−TiO_2 coatings obtained on AZ91D magnesium alloy by a chromium-free process [J]. Surfaces and Interfaces, 2020, 21: 100733.

[11] RAJABALIZADEH Z, SEIFZADEH D, HABIBI-YANGJEH A, MESRI GUNDOSHMIAN T, NEZAMDOUST S. Electrochemical noise analysis to examine the corrosion behavior of Ni−P deposit on AM60B alloy plated by Zr pretreatment [J]. Surface and Coatings Technology, 2018, 346: 29−39.

[12] SEIFZADEH D, FARHOUDI L. Electroless Co−P plating on magnesium alloy and its anti-corrosion properties [J]. Surface Engineering, 2016, 32: 348−355.

[13] FENG Li, WEN Cen, LI Jia-feng, LI Si-zhen, CHENG De, BAI Jing-ying, CUI Qin-xin. Effect of $Na_4P_2O_7{\cdot}10H_2O$ as complexing agent on deposition behavior and property of electroless Ni−P coating on ZK61M magnesium alloy [J]. Materials Research Express, 2019, 6: 56548.

[14] IRANIPOUR N, AZARI KHOSROSHAHI R, PARVINI AHMADI N. A study on the electroless Ni−P deposition on WE43 magnesium alloy [J]. Surface and Coatings Technology, 2010, 205: 2281−2286.

[15] SEIFZADEH D, MOHSENABADI H K. Corrosion protection of AM60B magnesium alloy by application of electroless nickel coating via a new chrome-free pretreatment [J]. Bulletin of Materials Science, 2017, 40: 407−415.

[16] LIU Zhen-min, GAO Wei. The effect of substrate on the electroless nickel plating of Mg and Mg alloys [J]. Surface and Coatings Technology, 2006, 200: 3553−3560.

[17] AMBAT R, ZHOU W. Electroless nickel-plating on AZ91D magnesium alloy: Effect of substrate microstructure and plating parameters [J]. Surface and Coatings Technology, 2004, 179: 124−134.

[18] QIN Tie-nan, MA Li-qun, YAO Yan, NI Cong, ZHAO Xiang-yua, DING Yi. An in situ measure method to study deposition mechanism of electroless Ni-P plating on AZ31 magnesium alloy [J]. Transactions of Nonferrous Metals Society of China, 2011, 21: 2790−2797.

[19] FELIU JR S, PARDO A, MERINO M C, COY A E, VIEJO F, ARRABAL R. Correlation between the surface chemistry and the atmospheric corrosion of AZ31, AZ80 and AZ91D magnesium alloys [J]. Applied Surface Science, 2009, 255: 4102−4108.

[20] PAN Fu-sheng, MAO Jjian-jun, CHEN Xian-hua, PENG Jian, WANG Jing-feng. Influence of impurities on microstructure and mechanical properties of ZK60 magnesium alloy [J]. Transactions of Nonferrous Metals Society of China, 2010, 20: 1299−1304.

[21] RUSSIBA A, BEN ARTAY A, SHTECHMAN A, IFERGAN S, KUPIEC M. Grain refinement of AZ31 and ZK60 Mg alloys — Towards superplasticity studies [J]. Materials Science and Engineering A, 2001, 302: 56−62.

[22] ZHANG Zhen-ya, YANG Rui, CHEN Gang, ZHAO Yu-tao, SHAO Yang. Correlation between microstructure and tensile behavior in powder metallurgy ZK60 alloys [J]. Materials Letters, 2012, 89: 166−168.

[23] SILVA E P, MARQUES F, NOSSA T S, ALFARO U, PINTO H C. Impact of Ce-base mischmetal on the microstructure and mechanical behavior of ZK60 magnesium casting alloys [J]. Materials Science and Engineering A, 2018, 723: 306−313.

[24] LI X, QI W. Effect of initial texture on texture and microstructure evolution of ME20 Mg alloy subjected to hot rolling [J]. Materials Science and Engineering A, 2013, 560: 321−331.

[25] LI Jian-zhong, HUANG Jiu-gui, TIAN Yan-wen, LIU Chang-sheng. Corrosion action and passivation mechanism of magnesium alloy in fluoride solution [J]. Transactions of Nonferrous Metals Society of China, 2009, 19: 50−54.

[26] LEI Xi-ping, YU Gang, GAO Xiao-lian, YE Li-yuan, ZHANG Jun, HU Bo-nian. A study of chromium-free pickling process before electroless Ni−P plating on magnesium alloys [J]. Surface and Coatings Technology, 2011, 205: 4058−4063.

[27] BARAJAS J D, JOYA J C, DURAN K S, HERNANDEZ-BARRIOS C A, COY A E, VIEJO F. Relationship between microstructure and formation-biodegradation mechanism of fluoride conversion coatings synthesised on the AZ31 magnesium alloy [J]. Surface and Coatings Technology, 2019, 374: 424−436.

[28] PANEMANGALORE D B, SHABADI R, GUPTA M, JI G. Effect of fluoride coatings on the corrosion behavior of Mg−Zn−Er alloys [J]. Surfaces and Interfaces, 2019, 14: 72−81.
[29] FINTOVA S, DRABIKOVA J, HADZIMA B, TRSKO L, BREZINA M, DOLEZAL P. WASSERBAUER J. Degradation of unconventional fluoride conversion coating on AZ61 magnesium alloy in SBF solution [J]. Surface and Coatings Technology, 2019, 380: 125012.
[30] WU Li-ping, DONG Jun-hua, KE Wei. Potentiostatic deposition process of fluoride conversion film on AZ31 magnesium alloy in 0.1 M KF solution [J]. Electrochimica Acta, 2013 105: 554−559.
[31] CASANOVA P Y, JAIMES K J, PARADA N J, HERNANDEZ-BARRIOS C A, APARICIO M, VIEJO F, COY A E. Synthesis and evaluation of MgF_2 coatings by chemical conversion on magnesium alloys for producing biodegradable orthopedic implants of temporary use [J]. Journal of Physics: Conference Series, 2013, 466: 1−4.
[32] KEONG K G, SHA W, MALINOV S. Crystallisation kinetics and phase transformation behaviour of electroless nickel−phosphorus deposits with high phosphorus content [J]. Journal of Alloys and Compounds, 2002, 334: 192−199.
[33] SANKARA NARAYANAN T S N, BASKARAN I, KRISHNAVENI K, PARTHIBAN S. Deposition of electroless Ni−P graded coatings and evaluation of their corrosion resistance [J]. Surface and Coatings Technology, 2006, 200: 3438−3445.
[34] ZULETA A A, CORREA E, CASTANO J G, ECHEVERRIA F, BARON-WIECHEC A, SKELDON P, THOMPSON G E. Study of the formation of alkaline electroless Ni−P coating on magnesium and AZ31B magnesium alloy [J]. Surface and Coatings Technology, 2017, 321: 309−320.
[35] LIU Hong, QIAN Dai-shu. Evaluation of residual stress and corrosion behaviour of electroless plated Ni−P/Ni−Mo−P coatings [J]. Transactions of Nonferrous Metals Society of China, 2018, 28: 2499−2510.
[36] CHEN Zhong, XU Xiao-da, WONG C C, MHAISALKAR S. Effect of plating parameters on the intrinsic stress in electroless nickel plating [J]. Surface and Coatings Technology, 2003, 167: 170−176.
[37] CHEN C J, LIN K L. Internal stress and adhesion of amorphous Ni−Cu−P alloy on aluminum [J]. Thin Solid Films, 2000, 370: 106−113.
[38] HINO M, MURAKAMI K, MITOOKA Y, MURAOKA K, KANADANI T. Effects of zincate treatment on adhesion of electroless Ni−P coating onto various aluminum alloys [J]. Transactions of Nonferrous Metals Society of China, 2009, 19: 814−818.
[39] SHOGHI P, SEIFZADEH D, GHOLIZADEH-GHESH-LAGHI M, HABIBI-YANGJEH A. Pretreatment-free Ni−P plating on magnesium alloy at low temperatures [J]. Transactions of Nonferrous Metals Society of China, 2018, 28: 2478−2488.
[40] XIE Zhi-hui, YU Gang, LI Ting-jing, WU Zhen-jun, HU Bo-nian. Dynamic behavior of electroless nickel plating reaction on magnesium alloys [J]. Journal of Coatings Technology and Research, 2012, 9: 107−114.
[41] MEZAMDOUST S, SEIFZADEH D, HABIBI-YANGJEH A. Nanodiamond incorporated sol−gel coating for corrosion protection of magnesium alloy [J]. Transactions of Nonferrous Metals Society of China, 2020, 30: 1535−1549.
[42] LI Jian-zhong, TIAN Yan-wen, HUANG Zhen-qi, ZHANG Xin. Studies of the porosity in electroless nickel deposits on magnesium alloy [J]. Applied Surface Science, 2006, 252: 2839−2846.

初始沉积行为对 ZK60 和 ME20 镁合金化学镀 Ni−P 镀层性能的影响

冯 立，张有玮，文 陈，李思振，李家峰，程 德，白晶莹，崔庆新，张立功

中国空间技术研究院 北京卫星制造厂有限公司，北京 100194

摘 要：镁合金材料组分与化学镀 Ni−P 合金镀层初始沉积行为密切相关。研究 ZK60 和 ME20 镁合金化学镀 Ni−P 镀层的初始沉积行为。研究结果显示，镁合金组分差异显著影响镀层初始沉积过程以及镀层的结合强度、耐蚀性能和晶体结构。镀层初始沉积均优先发生在两种镁合金基体表面沉淀颗粒上。而 ZK60 镁合金沉淀颗粒经 HF 活化后具有更高的化学活性，控制镀层的初始沉积速率。ME20 镁合金的初始沉积速率与基体表面 MgF_2 膜层的致密性有关，而非沉淀颗粒。由于初始沉积行为的差异，ZK60 镁合金镀层较 ME20 镁合金镀层具有更高的结合强度和更好的耐蚀性能。ZK60 和 ME20 镁合金表面镀层主要是晶体结构，且 ME20 镁合金镀层中混有少量的微晶结构。

关键词：ZK60 镁合金；ME20 镁合金；化学镀镍；初始沉积；结合强度；耐蚀性能

(Edited by Wei-ping CHEN)